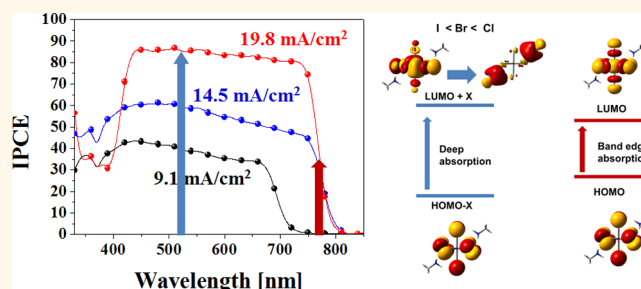


# Resonance Raman and Excitation Energy Dependent Charge Transfer Mechanism in Halide-Substituted Hybrid Perovskite Solar Cells

Byung-wook Park,<sup>†</sup> Sagar M. Jain,<sup>†</sup> Xiaoliang Zhang,<sup>†</sup> Anders Hagfeldt,<sup>†,§</sup> Gerrit Boschloo,<sup>\*,†</sup> and Tomas Edvinsson<sup>\*,‡</sup>

<sup>†</sup>Department of Chemistry-Ångström Laboratory, Physical Chemistry, Uppsala University, Box 523, SE 751 20 Uppsala, Sweden, <sup>‡</sup>Department of Chemistry-Ångström Laboratory, Inorganic Chemistry, Uppsala University, Box 538, SE 751 21 Uppsala, Sweden, and <sup>§</sup>Laboratory for Photomolecular Science (LSPM), Swiss Federal Institute of Technology at Lausanne (EPFL), CH-1015, Lausanne, Switzerland

**ABSTRACT** Organo-metal halide perovskites (OMHPs) are materials with attractive properties for optoelectronics. They made a recent introduction in the photovoltaics world by methylammonium (MA) lead triiodide and show remarkably improved charge separation capabilities when chloride and bromide are added. Here we show how halide substitution in OMHPs with the nominal composition  $\text{CH}_3\text{NH}_3\text{PbI}_2\text{X}$ , where X is I, Br, or Cl, influences the morphology, charge quantum yield, and local interaction with the organic MA cation. X-ray diffraction and photoluminescence data demonstrate that halide substitution affects the local structure in the OMHPs with separate  $\text{MAPbI}_3$  and  $\text{MAPbCl}_3$  phases. Raman spectroscopies as well as theoretical vibration calculations reveal that this at the same time delocalizes the charge to the MA cation, which can liberate the vibrational movement of the MA cation, leading to a more adaptive organic phase. The resonance Raman effect together with quantum chemical calculations is utilized to analyze the change in charge transfer mechanism upon electronic excitation and gives important clues for the mechanism of the much improved photovoltage and photocurrent also seen in the solar cell performance for the materials when chloride compounds are included in the preparation.



**KEYWORDS:** mixed halide perovskites · solution processing · solar cells · Raman spectroscopy · charge separation mechanism · density functional theory

Organo-metal halide perovskites (OMHPs) were first synthesized in 1978<sup>1,2</sup> but have received much scientific attention after their recent introduction as a photovoltaic material with very low cost and intriguing properties. The first report of use of OMHPs in a solar cell was made by Miyasaka *et al.* in 2009,<sup>3</sup> who used methylammonium lead triiodide ( $\text{MAPbI}_3$ ) and methylammonium lead tribromide ( $\text{MAPbBr}_3$ ) as absorber material deposited on mesoporous  $\text{TiO}_2$  in photoelectrochemical solar cells. Significant improvements in device performance and stability were found when the same materials were introduced in a solid-state dye-sensitized solar cell device structure, *i.e.*, in a structure where the liquid electrolyte was replaced

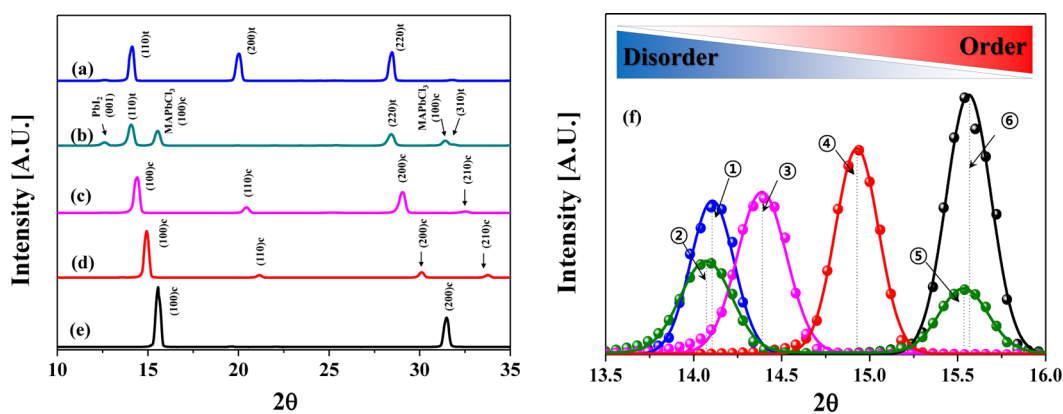
by a molecular hole conductor, and efficiencies close to 10% were reported in initial studies.<sup>4,5</sup> The power conversion efficiency (PCE) has significantly improved with the increased research efforts of recent years,<sup>6–9</sup> where Sang-il Seok and co-workers (Korea Research Institute of Chemical Technology, KRICT) hold the present record with 20.1% (certified).<sup>10</sup> It has become apparent that the organic–inorganic metal halide perovskites, and specifically  $\text{MAPbI}_3$  with addition of chloride, have many intriguing properties that need detailed investigation for a full understanding. One of the aspects that has raised a lot of speculation is the possible function of the much improved photocurrent and photovoltage when adding chloride to the system and in particular its effect

\* Address correspondence to gerrit.boschloo@kemi.uu.se, tomas.edvinsson@kemi.uu.se.

Received for review December 23, 2014 and accepted February 4, 2015.

Published online February 04, 2015  
10.1021/nn507345e

© 2015 American Chemical Society



**Figure 1.** Full XRD Diffractograms summarized for OMHPs, viz., (a) MAPbI<sub>3</sub>, (b) MAPbI<sub>2</sub>Br, (c) MAPbI<sub>2</sub>Cl, (d) MAPbBr<sub>3</sub>, and (e) MAPbCl<sub>3</sub>. (f) Extracted XRD patterns of preferred orientation in the range 13.0–16.5 2θ from XRD patterns of the left panel: ① MAPbI<sub>3</sub>, ② MAPbI<sub>3</sub> in MAPbI<sub>2</sub>Cl, ③ MAPbI<sub>2</sub>Br, ④ MAPbCl<sub>3</sub> in MAPbI<sub>2</sub>Cl, ⑤ MAPbBr<sub>3</sub>, ⑥ MAPbCl<sub>3</sub>.

on the interplay with the organic MA cation in the OMHP structure. Not only is it a rather bulky cation, it also has a dipole moment and protons that may be involved in hydrogen bonding. Furthermore, if the dipolar MA ion is liberated so it can rotate, it can contribute to a ferroelectric effect as well as a dynamic alignment and thus a more effective charge screening and separation. Here we address these issues with an investigation of the effects of the organic cation when using different halides in the OMHPs.

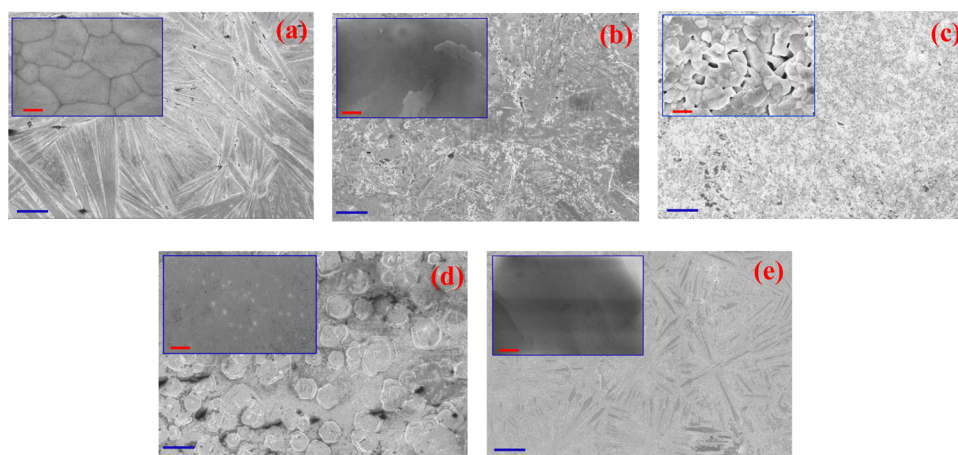
In other studies, partial substitution of the iodide in MAPbI<sub>3</sub>-based solar cells by introducing bromide (Br) and chloride (Cl) was found to improve the performance and stability of the devices.<sup>11–13</sup> Inclusion of bromide changes the crystalline phase of the OMHP from tetragonal to cubic for Br:I ratios larger than 1:4.<sup>11,14</sup> Small amounts of Cl in MAPbI<sub>3</sub> appear to increase the charge mobility.<sup>12,13</sup> It is, however, still largely unclear why Cl and Br inclusion leads to improved solar cell performance. Mosconi *et al.* performed computational calculations for the different trihalide modifications to MAPbX<sub>3</sub> (X = Cl, Br, I) and MAPbI<sub>2</sub>X, to investigate the role played by these halides in OMHPs with respect to the electronic, optical, and structural properties.<sup>15</sup> They suggested that hydrogen bonding between the ammonium groups and the halides in OMHPs is an important factor for the properties and stability of the materials.

We investigate the role of the halide by performing correlating investigations between chemical and physical properties for halide substitution in OMHPs during the preparation processes. Raman spectra for different crystalline phases of prototypical MAPbI<sub>3</sub> have recently been reported,<sup>16</sup> but the mechanistic function of the halides in the properties of the organic cation within an inorganic octahedron framework has so far been unclear. The crystalline growth through a disordered to ordered phase transition has previously been investigated in MAPbI<sub>3</sub> at different temperatures.<sup>17</sup> Here, we investigate the relationship between the inorganic

cage and an organic molecule for three substances during the synthesis process, namely, MAPbI<sub>3</sub>, MAPbI<sub>2</sub>Br, and MAPbI<sub>2</sub>Cl prepared with the respective methylamine halides (MAX), by cross-correlating X-ray diffraction (XRD), photoluminescence (PL), UV–visible spectroscopy, Raman spectroscopy, and density functional theory (DFT) calculations. In particular, the different halide-substituted OMHPs are investigated (see Figure 1) in order to understand the relationship between the local structure of OMHPs and the dynamics of the organic MA cation and the halides. These effects seem to be significantly related to charge separation and transport efficiency for thin-film solar cell systems of OMHPs.

## RESULTS

OMHP layers with the nominal compositions MAPbX<sub>3</sub> and MAPbI<sub>2</sub>X, where X is I, Cl, or Br, were deposited onto microscope glass by spin coating the precursor solution, followed by heating to 100 °C; see Methods section for details. XRD patterns of the resulting films are shown in Figure 1a and b. The MAPbI<sub>3</sub> film shows a tetragonal crystalline perovskite phase in good agreement with literature,<sup>8,17</sup> while MAPbBr<sub>3</sub> and MAPbCl<sub>3</sub> show a cubic structure. The XRD peak positions, calculated lattice distances (*d*-spaces), and crystal sizes from full width at half-maximum (fwhm) are summarized in Table S1. It is known that MAPb(I<sub>1-x</sub>Br<sub>x</sub>)<sub>3</sub> exists in a tetragonal phase for *x* < 20% of total halide and in the cubic phase for *x* > 20%.<sup>11</sup> In this study, MAPbI<sub>2</sub>Br (equimolar ratio between PbI<sub>2</sub> and MABr) was indeed found to be cubic, consistent with previous observations. MAPbI<sub>2</sub>Br shows a single-phase XRD pattern with a main peak assigned to (100)*c*, shifted 0.28° toward a higher angle compared to (110)*t* of MAPbI<sub>3</sub>. The OMHP with nominal composition MAPbI<sub>2</sub>Cl (equimolar ratio between PbI<sub>2</sub> and MACl) contained subcrystals of MAPbI<sub>3</sub> and MAPbCl<sub>3</sub>, but does not contain a halide mixed phase, which is in good agreement with previous investigations.<sup>12,13,17</sup>



**Figure 2.** Surface morphologies for (a) MAPbI<sub>3</sub>, (b) MAPbI<sub>2</sub>Br, (c) MAPbI<sub>2</sub>Cl, (d) MAPbBr<sub>3</sub>, and (e) MAPbCl<sub>3</sub> (the scale of black color: 40 μm) with inset figures magnifying each surface morphology (scale of red color: 200 nm).

In comparison, the integrated XRD intensities of the MAPbI<sub>3</sub> and MAPbCl<sub>3</sub> peaks in Figure 1f can demonstrate a crystal ratio of 1.5:1 for these two materials, in good agreement with the relation of the compounds in the preparation procedure. Some traces of crystalline PbI<sub>2</sub> with a (001) orientation were also found, similar to previous investigations.<sup>8</sup> It has been reported that residual PbI<sub>2</sub> may give rise to a passivation effect in OMHP solar cells.<sup>18</sup> In previous investigations,<sup>17,19</sup> the crystallinity of MAPbI<sub>3</sub> films, prepared under the same conditions as here, was only 30% at best, while the remainder was amorphous material. A slow crystallization process of self-assembly was found to proceed during weeks of aging such as second-order phase transition, which is related to thermodynamic entropy effects with crystalline growth.<sup>17</sup> In this investigation, we observe a first-order phase transition<sup>20,21</sup> owing to chemically substituted halides with a decreasing lattice spacing and increasing intensities in the order MAPbI<sub>3</sub>, MAPbI<sub>2</sub>Br, MAPbBr<sub>3</sub>, and MAPbCl<sub>3</sub>, as summarized in Table S1 and Figure 1f. In particular, subcrystallites of MAPbI<sub>3</sub> and MAPbCl<sub>3</sub>, during the mixed I/Cl halide preparation, are obtained with values of lattice spacing in good agreement with those of pure MAPbI<sub>3</sub> and MAPbCl<sub>3</sub> but with approximately 17% reduction in grain sizes. The lattice spacing is slightly shifted to lower angle with diminishing intensities, consistent with a disorder phase transition, agreeing with previously reported results.<sup>17</sup> The SEM images depicted in Figure 2a–e show that the halide modification in MAPbX<sub>3</sub> has a significant effect on the resulting surface morphologies of the perovskites. Although the crystal sizes estimated from XRD are quite similar (23–28 nm, see Table S1), the surface morphologies differ much in the submicrometer scale. MAPbI<sub>3</sub> displays smooth sections with irregular boundaries with a collective crystallite size of 200 to 600 nm. MAPbI<sub>2</sub>Cl films contain 180–190 nm sized crystals with mixed subcrystals of MAPbI<sub>3</sub> and MAPbCl<sub>3</sub> according to the XRD result. The MAPbI<sub>2</sub>Br and MAPbCl<sub>3</sub>

films appear very smooth in high magnification, whereas the MAPbBr<sub>3</sub> film shows hexagonal micrometer crystallites. The submicrometer scale, however, indicates very similar surface morphology to those of MAPbI<sub>2</sub>Br and MAPbCl<sub>3</sub>. The SEM cross sections of mixed halide OMHPs, shown in Figure 5a, confirm this.

The optical properties of MAPbI<sub>3</sub>, MAPbI<sub>2</sub>Br, and MAPbI<sub>2</sub>Cl films are shown in Figure 3. In the absorption spectra of MAPbI<sub>3</sub> and MAPbI<sub>2</sub>Cl an absorption onset at about 780 nm is found, corresponding to an optical band gap of about 1.6 eV, while that of MAPbI<sub>2</sub>Br appears at 690 nm, which corresponds to an optical band gap of about 1.8 eV, in good agreement with the trend reported by Noh *et al.*<sup>11</sup> In comparison to the MAPbI<sub>3</sub> film, in the MAPbI<sub>2</sub>Cl film (containing a two-phase mixture of MAPbI<sub>3</sub> and MAPbCl<sub>3</sub>) an increasing absorption can be seen at wavelengths below 470 nm and further below 410 nm, which can be attributed to absorption in the PbI<sub>2</sub> and MAPbCl<sub>3</sub> fractions in this material, respectively.<sup>6,17</sup>

Photoluminescence spectra for the same samples are shown in Figure 3b. MAPbI<sub>3</sub> has its peak emission at 775 nm (1.59 eV), while MAPbI<sub>2</sub>Br has a blue-shifted peak at 700 nm (1.77 eV), in agreement with the band gap values of these semiconductors. MAPbI<sub>2</sub>Cl has a significantly broadened emission spectrum, with a width at half-maximum approximately twice that of MAPbI<sub>3</sub>. A clear shoulder at 734 nm is found. The relative intensities of the photoluminescence were 1:2.5:6.5 for MAPbI<sub>3</sub>:MAPbI<sub>2</sub>Br:MAPbI<sub>2</sub>Cl, respectively. Apparently, Br substitution as well as the use of the Cl precursor leads to OMHP materials where less of the created excitons are lost due to nonradiative decay processes, like that of a direct band gap semiconductor.<sup>22</sup> Br substitution and a Cl precursor have an effect on the order of the inorganic sublattice but may also have an effect on the organic cation and the localization of excited-state charges, as investigated in more detail below.

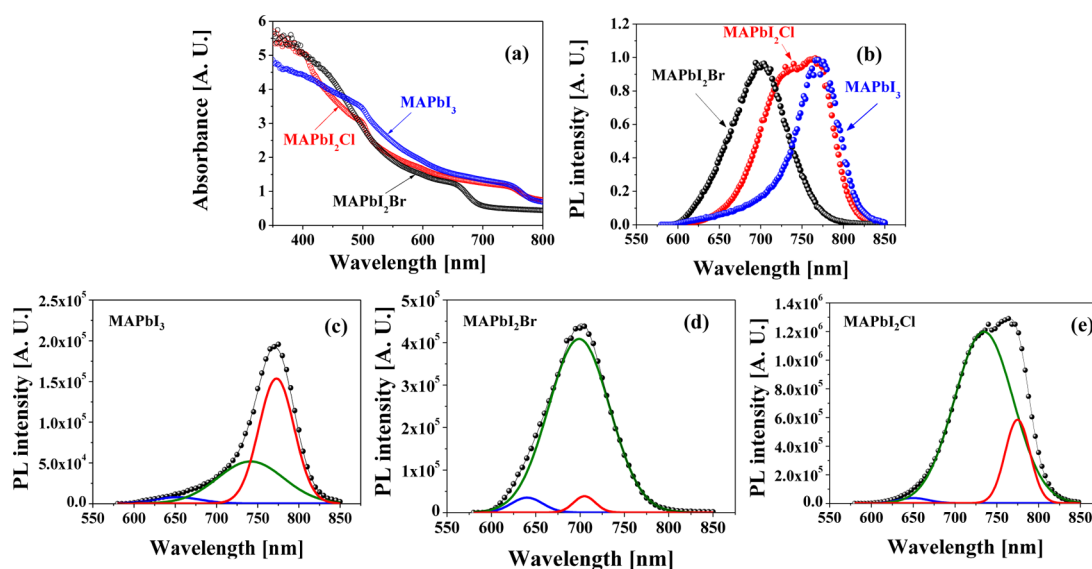


Figure 3. Optical properties of MAPbI<sub>3</sub>, MAPbI<sub>2</sub>Br, and MAPbI<sub>2</sub>Cl thin films on glass. (a) Electronic absorption spectra. (b) Normalized steady-state photoluminescence spectra (pump fluence wavelength at 610 nm). (c–e) Deconvoluted spectra.

The mechanism of changes in quantum efficiency has previously been investigated in inorganic light-harvesting materials by peak fitting PL spectra.<sup>23</sup> In the same way, the crystalline constitutions of OMHPs can be analyzed by fitting PL spectra with Gaussian functions using three components, as shown in Figure 3c–e. Corresponding phase transitions of crystalline parts have previously been investigated on other inorganic light-harvesting and metal oxide materials.<sup>24,25</sup> The blue curves of PL spectra in Figure 3c–e would then correspond to the optical band edge of orthorhombic-phased OMHPs assigned from the magnitude of the Stokes shift.<sup>26</sup> The two PL spectra of MAPbI<sub>3</sub> and MAPbI<sub>2</sub>Cl indicate two constitutions, represented by the red and green curves in Figure 3c and e, where the two kinds of local phases may be distinguished as ordered and disordered crystallites. The curves demonstrate different fwhm, one with a width of 70–80 nm (disorder) and one with less than 30 nm (order). Since the total emission is proportional to the area under the PL curve, a comparison between the integrated areas can give an estimation of the relative difference of the quenching yield of the photogenerated charge carriers. MAPbI<sub>3</sub> shows a ratio of charge quenching yield (integral PL spectra)<sup>27</sup> of 1:1.6 for disordered and ordered phases, respectively. We can note that the PL spectrum of MAPbI<sub>2</sub>Cl is not interfering with the fluorescence of MAPbI<sub>3</sub> due to the huge difference in the PL intensity between MAPbI<sub>2</sub>Cl and MAPbI<sub>3</sub> as seen in Figure s4. The ratio of the charge carriers effective for the PL emission is 5:1 with respect to disordered and ordered phases of MAPbI<sub>3</sub> within the MAPbI<sub>2</sub>Cl film. The energy shift of PL spectra for disordered and ordered phases in PbWO<sub>4</sub> monospecies has been addressed in the same

way as in a previous study.<sup>28</sup> Following the same reasoning and comparing the PL behavior of the MAPbI<sub>3</sub> and MAPbI<sub>2</sub>Cl materials, the effect of Cl-induced OMHP film formation can consequently result in a significantly higher effective charge lifetime. For the Br substitution, on the other hand, the PL spectrum of the green curve on MAPbI<sub>2</sub>Br indicates approximately 90% charge quenching yield, which can correspond to a disorder-phased crystallite, and the PL spectrum of the red curve can be assigned to an order-phased crystallite in Figure 3d.

The improved charge lifetime effect can thus be analyzed *via* the PL spectra and correlates with the order to disorder XRD patterns on bulk OMHPs. Nevertheless, the origin of the improved material properties by the halide-induced OMHPs is still not clear. We have therefore performed Raman spectroscopy on the given OMHP clusters to obtain information on local phase transitions and charge separation/transfer mechanisms. There have been some previous Raman spectroscopy studies on OMHPs, but peak assignment is ambiguous in these studies and also they do not include possibilities to study vibrations below 60 cm<sup>-1</sup>.<sup>16</sup> Theoretically calculating the exact Raman shift from quantum mechanics is notoriously problematic due to the low energies that are evaluated. Theoretical results within 5–10 cm<sup>-1</sup> from the experimental values are more a matter of coincidence, and the order of the vibration peaks can be problematic if there is no clear experimental spectrum to compare with. Here, we have performed low-frequency Raman measurements (down to 10 cm<sup>-1</sup>) and nonperiodic DFT calculations with emphasis on the ordering of the peaks to determine Raman properties of OMHPs. In particular, we investigate the fundamental vibrations

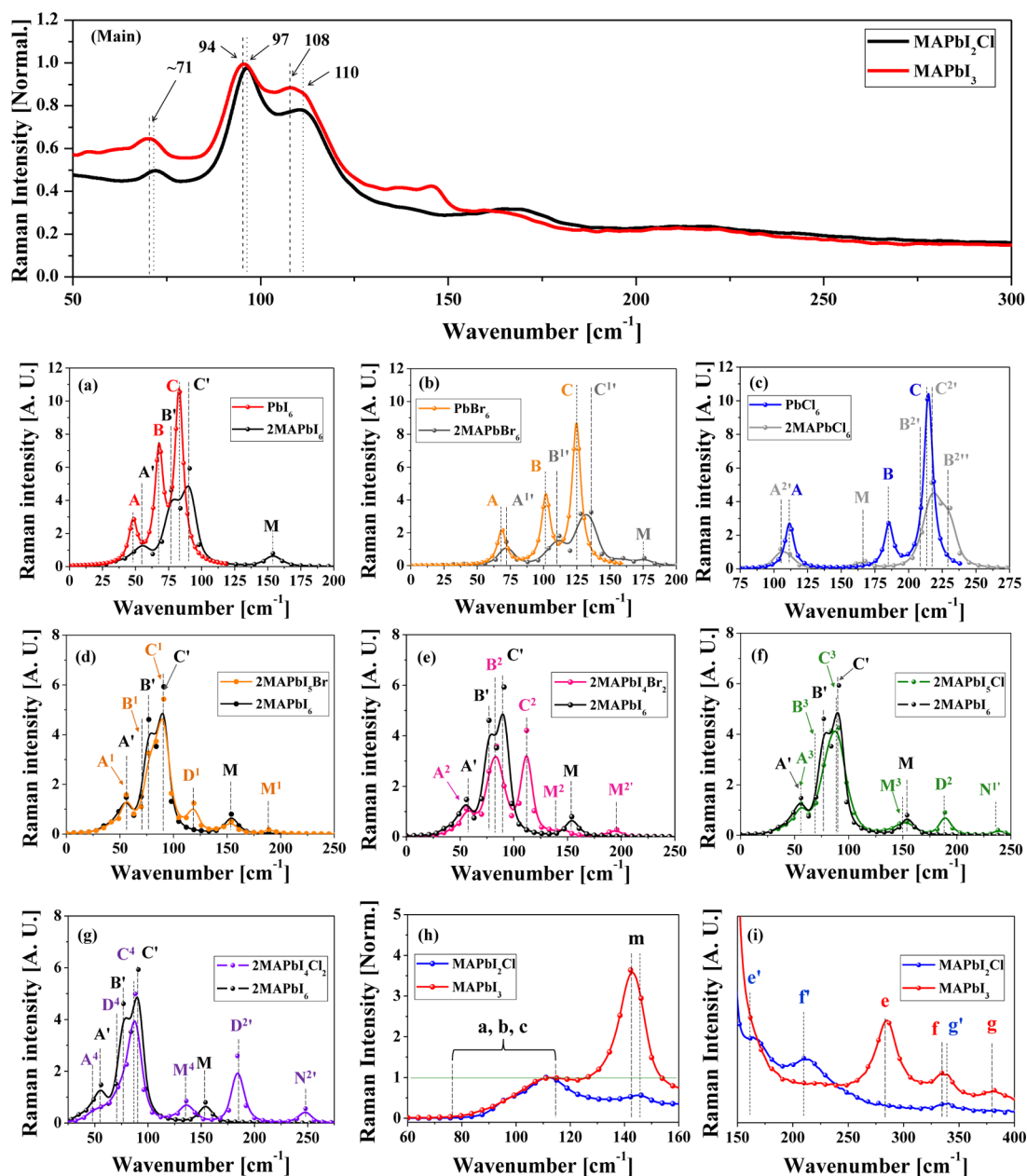
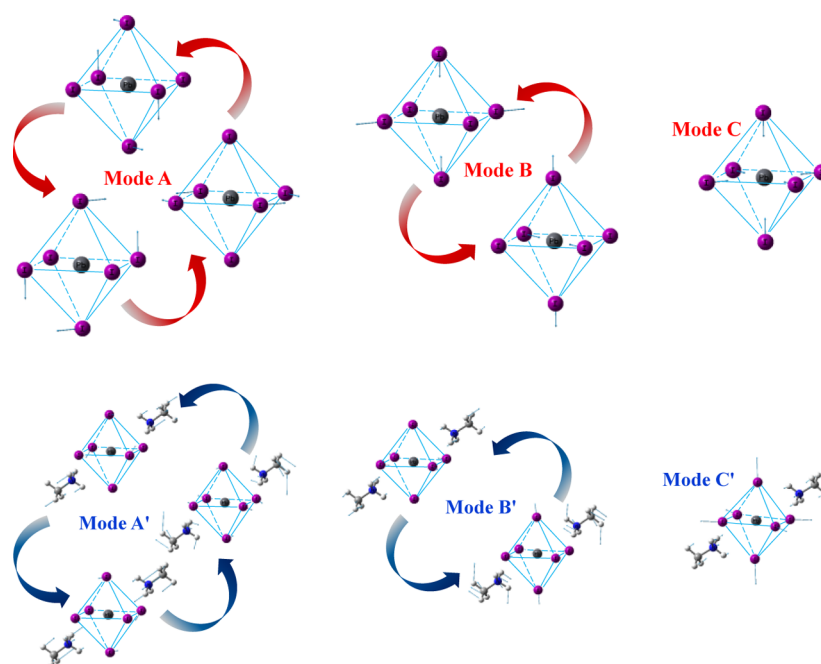


Figure 4. Experimental Raman spectra (main), DFT-calculated Raman spectra for (a)  $\text{PbI}_6$  with 2  $\text{MAPbI}_6$ , (b)  $\text{PbBr}_6$  with 2  $\text{MAPbBr}_6$ , and (c)  $\text{PbCl}_6$  with 2  $\text{MAPbCl}_6$ , and comparison of 2  $\text{MAPbI}_6$  with (d) 2  $\text{MAPbI}_6\text{Br}$ , (e) 2  $\text{MAPbI}_6\text{Br}_2$ , (f) 2  $\text{MAPbI}_6\text{Cl}$ , and (g) 2  $\text{MAPbI}_6\text{Cl}_2$ . (h, i) Normalized experimental Raman spectra recorded at very low laser intensity ( $<0.01$  mW).

in the isolated clusters and can follow the trends in the splitting of the degenerate states when different halogens are included in the structure. This can then form a strong basis for comparison with our experimental data as well as with previously performed periodic calculations.<sup>16</sup>

The experimental Raman spectrum for  $\text{MAPbI}_3$  shows vibration peaks at 40, (54), (63), 71, 94, 108, 135, and  $145\text{ cm}^{-1}$ , whereas  $\text{MAPbI}_2\text{Cl}$  shows corresponding peaks at 40, NA, NA, 71, 97, 110, and a broad peak at  $166\text{ cm}^{-1}$  as seen in Figure 4 (see Supporting Information for resolved peaks under  $60\text{ cm}^{-1}$ ). With the NA (not applicable) notation, we want to

emphasize that the peaks cannot be resolved and the spectra instead show a shoulder in that area. The 63 and  $94\text{ cm}^{-1}$  vibration peak is in good agreement with the 62 and  $94\text{ cm}^{-1}$  peak reported previously<sup>16</sup> for  $\text{MAPbI}_3$ , whereas our  $63\text{ cm}^{-1}$  peak is very weak, and our assignment instead shows that our stronger  $71\text{ cm}^{-1}$  peak is more likely to correspond to the significant mode in this area. Experimental spectra in the previous study, however, showed that other peaks below  $63\text{ cm}^{-1}$  were not resolved, making peak assignment problematic. Here we find peaks also at 40 and  $54\text{ cm}^{-1}$ , whereas the strongest Raman peaks are found at  $69\text{--}73$ ,  $94\text{--}97$ , and  $108\text{--}110\text{ cm}^{-1}$ , with a



**Scheme 1.** Three vibrational modes of inorganic octahedra (top figure) and bi-methylammonium-installed octahedra (bottom figure).

small shift depending on halide composition during synthesis. To assist with the assignment, we perform theoretical vibration spectroscopy with DFT. In periodic DFT calculations, assumptions about the crystal symmetry of the system have to be made. This then provides a good model system for single-crystalline materials where the different orientation of the cations must be considered to be periodic. For the study of local effects in the inorganic octahedron and a non-periodic or noncrystalline behavior of the organic cation, cluster calculations on the other hand can be very informative. In the present approach, an inorganic octahedron unit cluster  $\text{PbX}_6$  is used, and this cluster is combined with two MA-dipole canceling cations. A  $\text{PbI}_6$  octahedron has 15 internal degrees of freedom ( $3N - 3$ , where  $N$  is the number of iodine atoms). In a group theoretical representation,<sup>29</sup> they can be written as  $A_{1g} + E_g + 2T_{1u} + T_{2g} + T_{2u}$ , where  $A_{1g}$ ,  $E_g$ , and  $T_{2g}$  are Raman active, the two  $T_{1u}$  modes are IR active, and  $T_{2u}$  is a silent mode (neither Raman or IR active). Considering  $\text{PbI}_6$  as a molecular unit within the lattice, it belongs to the  $O_h$  symmetry group, and any deviation from this symmetry would result in splitting of the degenerate states and eventually complete removal of symmetry and 15 different bands. For Raman one would thus expect three bands for the fully  $O_h$  symmetric  $\text{PbI}_6$  and a splitting that would depend on the positions of the surrounding organic cations. Calculated Raman spectra for  $\text{PbX}_6$  and  $(\text{MA})_2\text{PbX}_6$  clusters are shown in Figure 4a–g, and experimental data for  $\text{MAPbI}_3$  and  $\text{MAPbI}_2\text{Cl}$  are shown in Figure 4h and i. Notably, Raman spectra of Br-containing OMHPs could not be obtained in the experiment, because of strong

fluorescence hiding the vibration information using either a 532, 633, or 785 nm laser. The calculated Raman signals for the octahedron clusters are summarized in Table S2, showing three different vibrational modes in Scheme 1: triply degenerate asymmetric X-Y, X-Z, and Y-Z vibrations (mode A), a double-degenerate asymmetric “breathing” (mode B), and symmetric “breathing” (mode C). Furthermore, the MA vibrations (rotation, wagging, MA–MA stretch) are shown. In agreement with the group theoretical analysis, we observe three bands for the unperturbed  $\text{PbX}_6$  clusters and a splitting of the degenerate states in the  $(\text{MA})_2\text{PbX}_6$  clusters into six Raman-active vibrations. The Raman peaks in  $(\text{MA})_2\text{PbX}_6$  clusters are generally shifted to higher wavenumbers (energy) compared to those in the  $\text{PbX}_6$  clusters, which is caused by the organic cations that extend the motion of X from the  $\text{Pb}^{2+}$  atom. Assuming an ideal iodine-sharing network vibrating fully in phase, the higher wavenumbers in the symmetric clusters would then approach the phonon vibration limit. The calculated Raman spectrum of  $(\text{MA})_2\text{PbCl}_6$  (see Figure 4c) differs somewhat from the other clusters. Mode A shifts to lower wavenumbers, and mode B appears as two peaks. Finally, all  $(\text{MA})_2\text{PbX}_6$  structures show Raman activity of the MA groups between 140 and  $180\text{ cm}^{-1}$ .

We also performed DFT calculations on mixed halide clusters, such as  $(\text{MA})_2\text{PbI}_5\text{Cl}$  and  $(\text{MA})_2\text{PbI}_4\text{Cl}_2$ . A single Cl substitution does not result in large differences in calculated Raman vibrational spectra compared to the  $(\text{MA})_2\text{PbI}_6$  cluster, while larger changes are found for two introduced Cl atoms. This can be used for

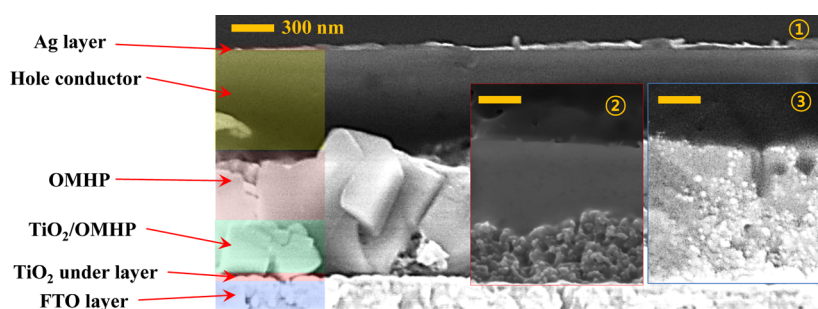


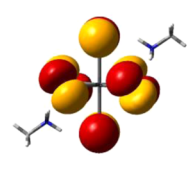
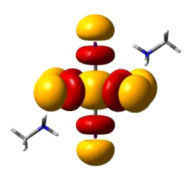
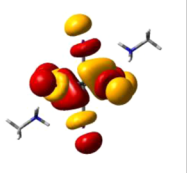
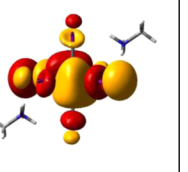
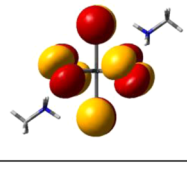
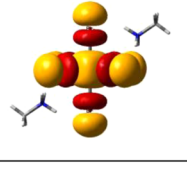
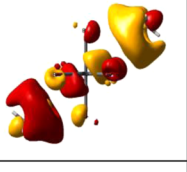
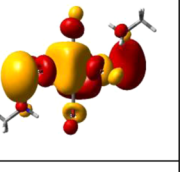
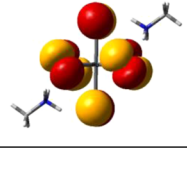
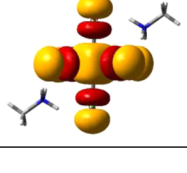

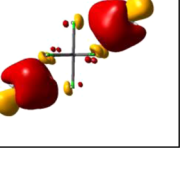
Figure 5. Cross sectional SEM images for thin-film solar cell devices (① MAPbI<sub>2</sub>Cl, ② MAPbI<sub>2</sub>Br, and ③ MAPbI<sub>3</sub> light-harvesting layers).

assignments and vibrational signatures (D) that can identify doped phases. Figure 4f and g show Raman activities compared to the (MA)<sub>2</sub>PbI<sub>6</sub> cluster, which is assigned to asymmetric vibrations of Pb–I between 40 and 95 cm<sup>-1</sup>. Moreover, there are two small appearances of additional vibration modes, for instance N<sup>1'</sup> (green color, N–Cl stretch *via* H at 240 cm<sup>-1</sup>) and D<sup>2</sup> (green color, Pb–Cl stretch at 190 cm<sup>-1</sup>) in Figure 4f. The case of (MA)<sub>2</sub>PbI<sub>4</sub>Cl<sub>2</sub> with double Cl substitution in the octahedral unit in Figure 4g has rather different vibration modes, *viz.*, mode D<sup>4</sup> (violet color, asymmetric Pb–Cl stretch, 75–82 cm<sup>-1</sup>) and highly increased intensity of mode D<sup>2'</sup> (violet color, asymmetric Pb–Cl stretch at 185 cm<sup>-1</sup>) compared with mode D<sup>2</sup> (green colored solid line in Figure 4f). Moreover, in Figure 4g the Raman activity of mode M<sup>4</sup> (violet color, at 138–143 cm<sup>-1</sup>) is shown to shift to lower wavenumber compared to mode M<sup>3</sup> (green color, Figure 4f), but mode N<sup>2'</sup> (violet color, at 247 cm<sup>-1</sup>) is shifted to higher wavenumber for mode M<sup>2'</sup> (green color, Figure 4f). The inclusion of new vibration signatures and the relative intensity shifts in the Raman activities of (MA)<sub>2</sub>PbI<sub>4</sub>Cl<sub>2</sub> compared to the undoped analogue can thus be used to identify if there is local halide substitution or if the different halides are in two different phases. Both the single- and double-Cl-substituted OMHPs have the common signature of a decreased Raman intensity of modes C<sup>3</sup> and C<sup>4</sup> (green and violet colors) compared to mode C' (black color).

We first compare the DFT-simulated Raman spectra for three vibrational modes and the experimental Raman signal of MAPbI<sub>3</sub>; see Figure 4a, h, and i. In MAPbI<sub>3</sub> three shoulders or peaks in the 70–120 cm<sup>-1</sup> range are found that are indicated with a, b, and c, which can be assigned to modes A, B, and C. Moreover, a further four peaks (m, d, e, and f) appear between 140 and 400 cm<sup>-1</sup>, which can be assigned to mode M vibrations: MA rotation, MA wagging, and symmetric MA–MA stretch, in good agreement with a cross correlation between isolated MAs and periodic calculations.<sup>16</sup> This agreement can partly be attributed to the small difference between the extended crystals as a corner-sharing octahedral framework and the isolated clusters. Care has to be taken, however, since

the cluster model emulates the crystal in only one direction, and only these vibrations should be taken as representative of the crystalline system. As mentioned earlier, also periodic calculations find vibrations at low wavenumbers, 62 and 94 cm<sup>-1</sup>. The low wavenumbers are in the same region as our calculated values and compare favorably to their experimental data, but they also found the strongest intensity at 119 cm<sup>-1</sup> on meso-MAPbI<sub>3</sub>, not assigned to the Pb–I system.<sup>30,31</sup> For our system we find a peak at 145 (143) and stronger bands at 167 (149, 154, and 156) and 217 (very weak theoretical transition) cm<sup>-1</sup> below 250 cm<sup>-1</sup> that are related to the MA cation, as assigned in Table s2. Comparing this to the Raman spectrum of MAPbI<sub>2</sub>Cl shows that the mode B as peak “b” shows peak shift to lower intensity. This phenomenon is significantly correlated with the results of XRD patterns and PL spectra, which show more disordered inorganic frameworks. According to Coslovich *et al.*,<sup>32</sup> higher Raman activities have been observed to increase the electron–phonon interaction between the central cationic metal and anionic oxygen. It was suggested to decrease the low-energy electronic conductivity on superconductive material in inorganic perovskites. In our study, we can consider this effect for MAPbI<sub>3</sub> and the sub-MAPbI<sub>3</sub> crystal in MAPbI<sub>2</sub>Cl on modes A and C in comparison. If the same reasoning would hold in the MAPbI<sub>2</sub>Cl sample, the observed enhancement is seen of two local electron–phonon interactions in modes A and C but also a slightly decreased electron–phonon interaction in mode B compared to the MAPbI<sub>3</sub> sample. In particular, a significantly different Raman intensity is distinguished in the range 136–150 cm<sup>-1</sup> that shows 1.3 times higher Raman intensity in the MAPbI<sub>3</sub> sample at 143 cm<sup>-1</sup> compared to what the MAPbI<sub>2</sub>Cl sample shows at 145 cm<sup>-1</sup>, as seen in Figure 4. From the previous assignment in Table s2, this would correspond to the rotation of the MA unit around its own axis and also close to the MA wagging. As the laser can affect the composition of materials with any volatile organic compound, very low laser intensities were instead used (<0.01 mW) in Figure 4h and i. Here the intensity is up to 7 times higher at ~145 cm<sup>-1</sup> for the MAPbI<sub>3</sub> sample compared to MAPbI<sub>2</sub>Cl. The Stokes

**TABLE 1. Orbital Charge Localization of Three Different Halide-Substituted OMHPs in 2MAPbX<sub>6</sub> Clusters by DFT Calculations**

	HOMO	LUMO	LUMO+1	LUMO+2
2MAPbI <sub>6</sub>				
2MAPBr <sub>6</sub>				
2MAPCl <sub>6</sub>				

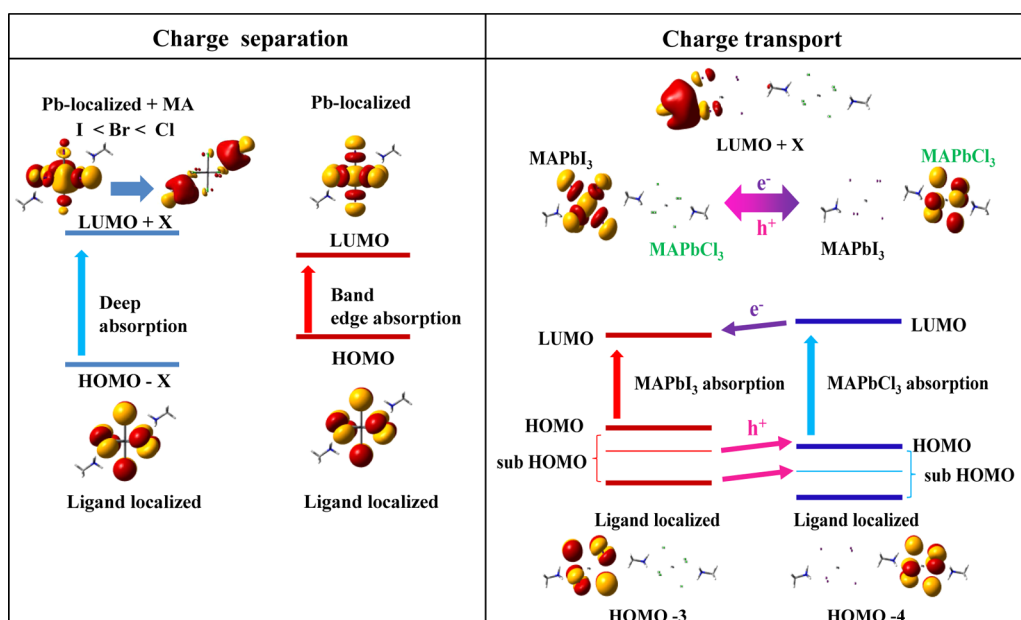
line in Raman measurements comes from the losses of the electromagnetic energy in the laser light to an excited vibration level in the bond where the intensity comes from the change in polarizability of the electron cloud during the vibration. The laser used for the Raman measurements on the OMHPs electronically excites the material, and we thus have a substantial resonance Raman effect enhancing the signal due to the electron cloud polarization from the excitation in the incoming electromagnetic field. During illumination, the perturbation Hamiltonian between the initial and final states,  $H_{if}$ , can be expressed in terms of how the incoming spatial electromagnetic field,  $A(r)$ , induces a displacement of the electron and thus in terms of the transition dipole moment,  $\mu_{if}$ , as in eq 1,

$$H_{if}' = -\frac{i\omega A}{m_0} \int \Psi_f^* e r \Psi_f d^3r = -\frac{1}{m_0} \mu_{if}' E_0 \quad (1)$$

where  $A$  is the incoming spatial field,  $\omega$  is the angular frequency,  $\Psi_f^*$  is the complex conjugate wave function of the initial state,  $\Psi_f$  is the accepting wave function for the virtual state,  $m_0$  is the mass of an electron,  $e$  is the elementary charge of an electron,  $r$  is the displacement, and  $E_0$  is the polarization field in the direction of the dipole. Since the expectation value of the displacement for a small interaction volume is small compared to the wavelength, one can utilize the dipole approximation and thus the assumption of the independence of the spatial field  $A(r)$  for a small displacement  $r$ . The disappearance of the feature at  $143 \text{ cm}^{-1}$  during resonance excitation at  $532 \text{ nm}$  then implies that the initial and final state polarization disappears for the

corresponding Raman rotation/wagging in the MA cation. Note that the initial ( $i$ ) and final states ( $f$ ) are not the HOMO–LUMO (or valence band–conduction band) transition that is expected to occur at lower wavelengths ( $790 \text{ nm}$ ) but excitations deeper in the absorption spectrum ( $532 \text{ nm}$ ) and also where the devices show high IPCE values. The remarkable difference at  $143\text{--}145 \text{ cm}^{-1}$  between  $\text{MAPbI}_3$  and  $\text{MAPbI}_2\text{Cl}$  samples seems to correlate with local charge transfer yield. The implication for such an effect on the local charge localization can be investigated in the OMHPs by DFT simulation. In previous studies,<sup>33,34</sup> the highest occupied molecular orbital (HOMO) and the lowest unoccupied molecular orbital (LUMO) are demonstrated on a cluster level in  $\text{PbI}_6$  for  $\text{MAPbI}_3$ . In Table 1, our DFT simulation results for unit clusters of OMHPs display the transitions of charges from the HOMO to LUMO (with LUMO+1 and LUMO+2). The HOMO of  $2\text{MAPbI}_6$  indicates an I 5p  $\pi$ -bonding orbital, and its LUMO, LUMO+1, and LUMO+2 are decomposed to “Pb(6s)–I(5p)”  $\sigma$ -antibonding, “Pb(6p)–I(5p)”  $\sigma$ -antibonding, and “Pb(6s)–I(5p)”  $\sigma$ -antibonding orbitals. The observation of 7 times lower intensity for the  $143 \text{ cm}^{-1}$  mode in the case of the  $\text{MAPbI}_2\text{Cl}$  sample corresponds to a loss of polarization on mode M (m in experiments) of internal  $\text{MAPbI}_3$ . One reasonable explanation would be a photoexcited state that cannot change its polarizability as easily, such as an MA cation radical or neutral MA molecule. This state can then play an important role as an organic cation charge stabilizer or a neutral dipolar molecule in the cage of the inorganic framework. In a previous study by





Scheme 2. Schematic picture of the charge localization (left) and charge transfer processes (right).

Frost *et al.*,<sup>33</sup> the importance of macroscopic static dielectric response and dipole order of various organic cations for OMHPs was investigated by DFT calculation but not in view of a MA radical but instead the dipole effect. A much improved charge stabilization in layered zirconium phosphonate-viologen compounds (ZrPV(X), with X = Br, Cl) has previously been suggested to be *via* the creation of a phosphonate-viologen radical cation.<sup>35</sup> Also here, the effect was much improved when going from a heavier halogen to a lighter halogen, suggested to be an effect of delocalization of the charges onto the organic cation and shielding from molecular oxygen.

In order to investigate the improved possibility of MA stabilizing a charge at higher excitations, DFT calculations were performed. The HOMO, LUMO, LUMO+1, and LUMO+2 of a dipolar canceling and stoichiometric cluster of (MA)<sub>2</sub>PbI<sub>6</sub>, (MA)<sub>2</sub>PbBr<sub>6</sub>, and (MA)<sub>2</sub>PbCl<sub>6</sub> are shown in Table 1 and Scheme 2 (left panel). For all the clusters, a ligand-to-metal charge transfer is seen for the HOMO–LUMO transition, where the initial localization on the iodine in the HOMO state is significantly transferred to the Pb central unit in the LUMO state. From the discussion above on the resonance Raman effect at 532 nm exciting the material to higher energy levels than the LUMO, we need to look at higher unoccupied states. Looking at LUMO+2, we see no localization on the MA cations in the (MA)<sub>2</sub>PbI<sub>6</sub> but some partial occupation for (MA)<sub>2</sub>PbBr<sub>6</sub> and a very clear localization on the MA cation for (MA)<sub>2</sub>PbCl<sub>6</sub>. The DFT calculations thus give strong support for improved charge localization at the MA cation for high unoccupied states in the series I → Br → Cl. If the MA cation also is more liberated to rotate in this state due to charge neutrality, this would also improve its

possibilities to align and work better in forming a ferroelectric system. Consequently, Br (or Cl) atom substituted MAPbX<sub>3</sub> can thus enhance the ferroelectric properties caused by ordering of the MA molecule due to the much improved freedom to rotate for a neutral dipolar molecule compared to its more positively charged analogue in 2MAPbI<sub>6</sub>. An important but maybe not obvious effect is also that the dipole of the neutral MA is stronger than the positively charged analogue MA<sup>+</sup>. DFT calculations for isolated molecules at the B3LYP/6-311G(d,p) level show a dipole of 2.22 D for the positively charged MA<sup>+</sup> and 3.02 D for the neutral MA.

The external quantum efficiency can be described by factorization of the incident-photon-to-current-efficiency (IPCE), as in eq 2.

$$\text{IPCE}(\lambda) = \text{LHE}(\lambda) \times \Phi_{\text{sep}}(\lambda) \times \Phi_{\text{trans}}(\lambda) \times \eta_{\text{coll}} \quad (2)$$

where  $\lambda$  is the wavelength of the light, LHE is the light-harvesting efficiency,  $\Phi_{\text{sep}}$  is the quantum efficiency for charge separation,  $\Phi_{\text{trans}}$  is the quantum efficiency for transport, and  $\eta_{\text{coll}}$  is the charge collection efficiency of the charges at the contact materials. The results presented here give support for an excitation-dependent charge separation mechanism where  $\Phi_{\text{sep}}(\lambda_{\text{band-edge}})$  is dominated by halogen-to-lead charge separation, whereas absorption at higher excitation energies  $\Phi_{\text{sep}}(\lambda_{\text{deep-abs}})$  show a successively larger influence of halogen-to-cation charge transfer in the series I → Br → Cl.

As discussed above, liberation of the MA cation and also the higher dipole of a neutral MA in the excited state would also have consequences for the possibility to align the MA dipoles and thus also for local fields affecting the charge transport of the

steady-state current flowing through the solar cell device. To investigate this effect in an idealized model system, we performed calculations on two model systems with extended clusters,  $\text{AMPbI}_6\text{-MA-PbI}_6\text{-AM}$  and  $\text{AM-PbCl}_6\text{-MA-PbI}_6\text{-AM}$ , with two MA cations having a dipole-canceling effect on the first cluster and two ordered dipoles in a row for the second cluster, depicted in Table s4. The ligand-to-metal charge transfer is now instead from the ligands in the initial cluster to a more metal-centered state in the neighboring cluster. As expected, the alignment of the MA dipole improves the hopping mechanism in the direction of the dipole. In a solar cell working at full illumination and with light that also includes higher wavelengths than the limiting HOMO–LUMO transition, higher states are of course active both in the charge separation mechanism (as we have discussed earlier) and for the transport up to LUMO+2. MA does not seem to contribute to a viable path for charge transport, but for LUMO+5 we see accepting orbitals also on the MA cations, as seen also for the smaller clusters. The absorption edge transition charge separation and transport mechanisms thus seem to be dominated by the ligand-to-metal transitions and hopping between the clusters mediated in the direction of the MA dipole, whereas at lower wavelengths in the region of the high IPCE values, the stabilization of the charges at the MA cation seems to be more important. Charge localization on MA at higher virtual orbitals is found also for the system with only iodine as seen in Table s4. Also the lower states, HOMO–1, HOMO–2, etc., are important, as the electrons are excited at higher energies than the HOMO–LUMO limiting transition. The initial creation of a hole would then be described by the lack of electron density previously found in the state. After some time under pulsed light or very weak light intensity, bond-length relaxation with the new electron configuration would occur and eventually higher state electrons would relax into the lower states and restore the original bond-length distribution. Under solar illumination and full working conditions, however, the low states, as well as the higher states, will continuously be excited and a steady-state condition of empty lower states can form a hole-conductive pathway in the system. The electron-conducting states will predominantly be described by the virtual orbitals, and the hole-conducting states by the empty HOMO and lower lying states. In Table s4, the initial localizations of electrons that can be lost under excitation are depicted. The electron localization clearly shows that steady-state excitation of these states will exclusively take part with localization at the iodine-ligand positions that are percolating in the crystalline OMHPs *via* sharing of iodine. This can be contrasted with the electron transport that is predominantly occurring *via* more Pb-localized states close to the HOMO–LUMO transition and localized at the MA cations for

higher transitions in the absorption spectra. The mechanism ruling the quantum efficiency for transport,  $\Phi_{\text{trans}}(\lambda)$ , in eq 2, thus also reveals an energy dependence.

We especially observe the notable local HOMO–HOMO transition possible between  $\text{PbI}_6$  and  $\text{PbCl}_6$  units below the HOMO–1 for a cluster of  $\text{MA-PbI}_6\text{-MA-PbCl}_6\text{-MA}$  in Table s4. This electron transition can consequently be assisting charge transfer with local charge pumping processes *via* higher and lower sub-HOMO states and, as such, affect the LHE factor in eq 2.

The photovoltaic properties of OMHPs with nominal compositions  $\text{MAPbI}_3$ ,  $\text{MAPbI}_2\text{Br}$ , and  $\text{MAPbI}_2\text{Cl}$  were also tested. SEM cross sections of fabricated thin-film solar cell devices are shown in Figure 5. The highly crystalline nature of the  $\text{MAPbI}_2\text{Cl}$  material is clear. In comparison,  $\text{MAPbI}_3$  and  $\text{MAPbI}_2\text{Br}$  layers look much more smooth and amorphous. The solar cell performance was best for  $\text{MAPbI}_2\text{Cl}$  devices, as is evident from the  $J$ – $V$  curves under 1 sun illumination in Figure 6a. The solar cell efficiencies were 5.8% for  $\text{MAPbI}_3$  (FF: 0.50,  $V_{\text{oc}}$ : 0.77 V,  $J_{\text{sc}}$ : 15.0  $\text{mA}/\text{cm}^2$ ), 3.2% for  $\text{MAPbI}_2\text{Br}$  (FF: 0.43,  $V_{\text{oc}}$ : 0.80 V,  $J_{\text{sc}}$ : 9.3  $\text{mA}/\text{cm}^2$ ), and 10.0% for  $\text{MAPbI}_2\text{Cl}$  (FF: 0.50,  $V_{\text{oc}}$ : 1.0 V,  $J_{\text{sc}}$ : 20.4  $\text{mA}/\text{cm}^2$ ). Incident photon to photocurrent conversion efficiency spectra (see Figure 6b) also show the best performance for  $\text{MAPbI}_2\text{Cl}$ , with IPCE values reaching nearly 85%. The integrated photocurrent values (Figure 6b) are calculated from the IPCE spectra and are in good agreement with the experimental short-circuit current densities measured in the solar simulator. The extrapolated onset wavelength from the IPCE spectrum is 800 nm for  $\text{MAPbI}_3$ , 785 nm for  $\text{MAPbI}_2\text{Cl}$ , and 720 nm for  $\text{MAPbI}_2\text{Br}$ , in accordance with the optical band gaps in Figure 6c. The  $\text{MAPbI}_2\text{Br}$  solar cell showed the lowest current density among the samples due to the lowest light-harvesting efficiency from UV–vis spectra and the lowest bulk conductivity. On the other hand, it indicates the possibility for higher  $V_{\text{oc}}$  from longer charge carrier lifetime  $\tau$  from PL intensity (and higher local polarizability) than the corresponding  $\text{MAPbI}_3$  as mentioned above. The  $\text{MAPbI}_2\text{Cl}$  solar cell showed the highest  $V_{\text{oc}}$  and  $J_{\text{sc}}$  as 1.0 V and 20.40  $\text{mA}/\text{cm}^2$ , respectively, which can be attributed to the longest charge carrier lifetime and a high ferroelectric property and thus an enhanced local conductivity caused by the stabilization of charges of MA cations as discussed above. All solar cell performances are in good agreement with our more detailed results on the effect of local charge stabilization at the MA in the series  $\text{I} > \text{Br} > \text{Cl}$  in OMHPs and its effects on the ordering of the MA cation.

Interestingly,  $\text{MAPbI}_2\text{Cl}$  has a dip as zone A in the IPCE spectrum below 430 nm in Figure 6c, which can be attributed to competitive light absorption by the  $\text{MAPbCl}_3$  crystals in this material in Figure 6d, which

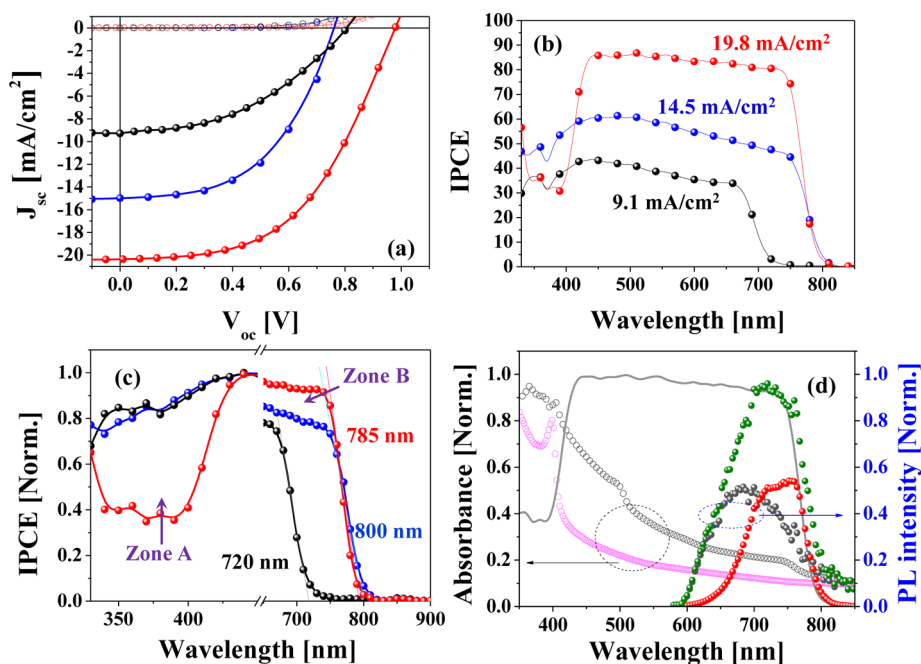


Figure 6. Summarized solar cell performances: (a)  $J$ – $V$  characterization, (b) IPCE curves, (c) normalized IPCE curves for MAPbI<sub>3</sub> (blue solid line), MAPbI<sub>2</sub>Br (black solid line), and MAPbI<sub>2</sub>Cl (red solid line) utilized solar cell devices. (d) Normalized UV–vis and PL spectra for MAPbCl<sub>3</sub> (pink and red round symbols) and MAPbI<sub>2</sub>Cl (dark gray round symbols). Sum of PL spectra (green round symbols) from two given samples; gray solid line is an IPCE curve of MAPbI<sub>2</sub>Cl.

apparently does lead to low photocurrent. On the other hand, the increase in the IPCE curve as zone B is observed and is an interesting phenomenon. We fortunately have the results on the charge transfer mechanism in the DFT calculation above. The existence of a PbCl<sub>6</sub> unit in connection to a PbI<sub>6</sub> unit would allow for a charge pumping property at a low HOMO level. This would lead to an improved charge excitation from the rising sub-HOMO level to the LUMO. This process would then explain the huge difference of IPCE at 600–800 nm wavelength as zone B and help to enhance the local charge carrier lifetime (see Scheme 2 (right panel)); the normalized PL spectra for MAPbCl<sub>3</sub> and MAPbI<sub>2</sub>Cl with the sum of PL spectra are summarized in Figure 6d. We thus find a possible charge-pumping processes between MAPbCl<sub>3</sub> (insulator) and MAPbI<sub>3</sub> (semiconductor) sub-crystallites within MAPbI<sub>2</sub>Cl. To further analyze this and the role of charge pumping requires more detailed experiments and is an interesting scope for future work.

## CONCLUSIONS

In summary, we observe a change in the local structure of I, Br, and Cl in the OMHPs from XRD and Raman measurements. MAPbI<sub>2</sub>Br-based solar cells show higher  $V_{oc}$  than MAPbI<sub>3</sub>, and this can be from the effect of enhanced antiferroelectric properties, as indicated by a 3 times enhancement of the charge carrier lifetime as measured with PL compared to MAPbI<sub>3</sub>. Here we have investigated MAPbI<sub>2</sub>Cl in more

detail and show two sub-crystallites, MAPbI<sub>3</sub> and MAPbCl<sub>3</sub>. These crystallites show a change in the local structure compared to the MAPbI<sub>3</sub> reference sample. The disordered octahedral framework of MAPbI<sub>3</sub> with a liberated MA cation has a remarkably longer charge lifetime than MAPbI<sub>3</sub> with an ordered MA cation. Furthermore, the disordered MAPbI<sub>3</sub> induced by addition of chlorine shows an up to 7 times lower change in polarizability and thus a deactivated mode M (m). This can be understood by an increased charge localization on the MA cation upon excitation and thus improves the possibilities for dipole alignment in response to a local field and thus enhanced ferroelectric properties. Results from DFT calculations on model clusters support this picture and show an excitation energy dependent mechanism for the charge transfer. The near-band-edge transition is dominated by an iodide to lead transition (ligand-to-metal), whereas the higher virtual states show a successively higher localization on the MA cation in the series I–Br–Cl. The lower sub-HOMO states exclusively show iodide (ligand) and chloride (ligand) localized states in close range, making a sub-HOMO pumping process possible, which can explain the increasing IPCE in the 600–800 nm range for MAPbI<sub>2</sub>Cl in comparison to MAPbI<sub>3</sub>. The material properties analyzed are well justified by the device performance, showing 1.7 times higher PCE with inclusion of chlorine compared to that of MAPbI<sub>3</sub> solar cells. Here, we have presented an excitation-dependent mechanistic view of the heterojunction charge localization and transfer between MAPbI<sub>3</sub> and

MAPbCl<sub>3</sub> within local MAPbI<sub>2</sub>Cl crystallites, which can possibly open up a new understanding of the nature

of OMHP materials in hybrid thin-film solar cell applications.

## METHODS

**Material Preparation.** Organic lead halide hybrid perovskites (OMHPs) were prepared by a low-temperature melting method from different precursor solutions. The starting materials were PbI<sub>2</sub> (purity 99%, Sigma-Aldrich), methylamine solution (40% in methanol, TCI), hydrochloric acid (37 wt % in water, Aldrich), hydroiodic acid (57 wt % in water, Aldrich), and hydrobromic acid (48 wt % in water, Aldrich). CH<sub>3</sub>NH<sub>3</sub>Cl, CH<sub>3</sub>NH<sub>3</sub>Br, and CH<sub>3</sub>NH<sub>3</sub>I were synthesized by mixing hydrogen halide acids with methylamine solution in equal molar ratio in a 250 mL round-bottom flask at 0 °C for 2 h with stirring. The precipitate was recovered by evaporation at 50 °C for 1 h. The products were washed in diethyl ether by stirring the solution for 30 min, which was repeated three times, and then finally dried at 60 °C in a vacuum oven for 24 h. The obtained CH<sub>3</sub>NH<sub>3</sub>Cl, CH<sub>3</sub>NH<sub>3</sub>Br, or CH<sub>3</sub>NH<sub>3</sub>I salts were mixed with PbI<sub>2</sub> (purity 98.0% Sigma-Aldrich), PbBr<sub>2</sub> (purity 98.0% Sigma-Aldrich), or PbCl<sub>2</sub> (purity 98.0%, Sigma-Aldrich) in a 1:1 molar ratio in a mixture of dimethylformamide (DMF) and dimethyl sulfoxide (DMSO) (7:3 = vol/vol) at 70 °C for 2 h. The concentration of the resulting precursor is 1.5 M. The OMHP precursors of MAPbI<sub>3</sub>, MAPbBr<sub>3</sub>, MAPbCl<sub>3</sub>, MAPbI<sub>2</sub>Br, and MAPbI<sub>2</sub>Cl were deposited on different substrates by a spin-coating method at 1500 rpm ( $\pm 25$  rpm) for 20 s. After spin-coating OMHPs precursor films were annealed on a hot plate at 100 °C for 35 min under dry air conditions (relative humidity below 30%). Mesoporous TiO<sub>2</sub> films were prepared by diluting TiO<sub>2</sub> paste (Dyesol, DSL 30 NRD) with 2-propanol (1:4 by weight) and spin-coating at 3000 rpm for 20 s, resulting in films of 450 nm ( $\pm 50$  nm) thickness after annealing at 450 °C.

**X-ray Diffraction.** The crystallographic properties of the perovskite films deposited on mesoporous TiO<sub>2</sub>-coated microscopic slides or bare microscopic slides were investigated using XRD with a Siemens D5000 diffractometer apparatus with a Kristaller-Flex 710D X-ray generator using Cu K $\alpha$ 1 radiation (0.1540562 nm, fine-focus sealed tube source with a Gobel mirror) at room temperature. The Diffrac Plus XRD commander program was used to control the instrument. The instrument was set in "detector scan" mode, and the acquisition was done in  $\theta \approx 2\theta$  mode for every 0.02° increment over the Bragg angle range of 10–60°. The XRD patterns were fitted by the X'pert highScore program.

**Scanning Electron Microscopy (SEM).** SEM was performed on a Zeiss (Gemini 1550) microscope having a field emission electron source and an in-lens detector for secondary electrons. Top view images and cross sections of solar cell devices were recorded using a high tension of 5 kV. OMHPs were coated on ITO glass substrates for top view images.

**Raman Measurements.** Raman spectra were measured with a Renishaw InVia Raman spectrometer with 1 cm<sup>-1</sup> resolution using a frequency-doubled YAG laser (532 nm) and an 1800 lines/mm grating. A 50 $\times$  objective was used and gave a laser spot with 3–5  $\mu$ m diameter with 0.01–1 mW intensity on the sample depending on measurement mode. A notch filter was used for the Rayleigh (Plasma) line of the 532 nm laser and a notch filter cutting 10 cm<sup>-1</sup> into the Stokes part of the spectra. For each sample, 50 spectra were recorded in the range 10–400 cm<sup>-1</sup> with no apparent change in the spectra during the cycles. OMHPs were coated on microscope glass substrates.

**Steady-State Emission Measurements.** Standard steady-state emission spectra were obtained on a Fluorolog-3 instrument (Horiba Jobin Yvon) equipped with double-grating excitation and emission monochromators and a 450 W Xe lamp as a light source. The emission spectra were corrected for the spectral sensitivity of the detection system by using a calibration file of the detector response. Front-face illumination (30° with respect to the incident beam) was used to minimize inner-filter effects.

Excitation was done at 610 nm. OMHPs were coated on microscope glass substrates.

**UV–Vis–NIR Spectra Measurements.** UV–visible–NIR absorption spectra were recorded using a Cary 5000 UV–vis–NIR spectrophotometer (Varian, photometric accuracy is <0.00025 Abs, photometric range is 8 Abs). OMHPs were coated on microscope glass substrates, and the microscope glass was used as reference.

**Calculations.** The density functional theory calculations were performed within the Gaussian09 package<sup>36</sup> using the hybrid functional B3LYP with the 6-311G(d,p) basis set and the Stuttgart-Dresden effective core potentials (ECP) for the heavy heavy elements as well as for light elements where relative peak shifts were analyzed. The convergence criterion was set to 10<sup>-8</sup> hartrees, and quantum mechanical linear response calculations were used in subsequent calculations to obtain the theoretical Raman spectra.

### Fabrication and Performance of Measurement for Solar Cell Devices.

**Fabrication of Solar Cell Devices.** Solar cells were prepared for OMHPs with nominal compositions MAPbI<sub>3</sub>, MAPbI<sub>2</sub>Br, and MAPbI<sub>2</sub>Cl. Fluorine-doped tin oxide (FTO)-coated glass ( Pilkington TEC 15, 15  $\Omega/\square$ ) was patterned using an etching process with Zn powder and 2 M HCl diluted in water. Compact TiO<sub>2</sub> layers (thickness 30–60 nm) were deposited on the FTO substrate by spray pyrolysis on a hot plate (kept at 500–550 °C).<sup>35</sup> The prepared TiO<sub>2</sub> precursor was coated by a spin-caster at 4000 rpm ( $\pm 30$  rpm) for 20 s and annealed on a hot plate at 500 °C for 30 min. The OMHP precursor was also deposited by a spin-coater at 1250 rpm ( $\pm 25$  rpm) for 20 s and annealed at 135–145 °C for 30–40 min in a drybox at 20–40% humidity. The hole transporter spiro-MeOTAD was deposited by spin-coating at 1500 rpm for 20 s as described before (see ref 15). Finally, 150 nm thick silver electrodes were deposited on top of the devices by thermal evaporation at  $\sim 10^{-6}$  bar, through a shadow mask.

**Power Conversion Efficiency.** A Newport solar simulator (model 91160), giving light with AM 1.5 G spectral distribution, was calibrated using a certified reference solar cell (Fraunhofer ISE) to an intensity of 1000 W m<sup>-2</sup>. The electrical data were recorded with a computer-controlled digital source-meter (Keithley model 2400) with the scan direction from the open-circuit to short-circuit at a scan rate of 800–1250 mV s<sup>-1</sup>.<sup>38</sup> The solar cells were masked during the measurement with an aperture area of 0.126 cm<sup>2</sup> (round type of mask).

**Incident Photon to Current Conversion Efficiency.** The IPCE spectra were recorded with a computer-controlled setup comprising a xenon lamp (Spectral Products, ASB-XE-175), a monochromator (Spectral Products, CM110), and a Keithley multimeter (model 2700). The setup was calibrated with a certified silicon solar cell (Fraunhofer ISE) prior to the measurements. All DSCs were illuminated from the WE side with an aperture area of 0.126 cm<sup>2</sup> (round type of mask) using a black mask. The MAPbI<sub>3</sub>-deposited solar cell was measured without bias light, and MAPbI<sub>2</sub>Br- and MAPbI<sub>2</sub>Cl-utilizing solar cells were measured under each different bias light intensity of 0.05 and 0.09 sun.

**Conflict of Interest:** The authors declare no competing financial interest.

**Acknowledgment.** We thank the Swedish Energy Agency, the STandUP for Energy Program, the Swedish Research Council (VR), the Göran Gustafsson Foundation, and the Knut and Alice Wallenberg Foundation for financial support. T.E. thanks the Ångpanneförenings Research Foundation for financial support. B-w.P. thanks the members of the Korea Swedish Scientists and Engineers Association (KSSEA) for support and thanks, in particular, Taeja Kim-Björklund, chairman of the KSSEA and Korean Association in Sweden. Further thanks go to

Mr. Seockjeong Eom, Ambassador in the Embassy of the Republic of Korea in Sweden. B.w.P. prepared the starting materials, composed the OMHPs, fabricated the solar cell devices, analyzed the data from crystallography, PL spectra, Raman spectra, DFT calculations, and all solar cell properties ( $J$ - $V$  and IPCE curves), and participated in writing the manuscript; S.M.J. supported the fabrication of the solar cell devices and the preparation of OMHPs and participated in writing the manuscript. X.Z. performed the SEM experiments; A.H. guided the work and edited the manuscript; G.B. edited the manuscript and supervised; T.E. carried out the DFT calculations and Raman investigations, participated in writing the manuscript, and guided the work.

**Supporting Information Available:** Additional plots of the experimental Raman and PL spectra, XRD data, calculated Raman spectra, super-LUMO and sub-HOMO orbital localizations, and solar cell performances for many measurements on OMHP devices with error bars can be found in the Supporting Information. This material is available free of charge via the Internet at <http://pubs.acs.org>.

## REFERENCES AND NOTES

- Weber, D.  $\text{CH}_3\text{NH}_3\text{SnBr}_{3-x}$  ( $x = 0-3$ ), a Sn(II)-System with Cubic Perovskite Structure. *Z. Naturforsch.* **1978**, *33b*, 862-865.
- Weber, D.  $\text{CH}_3\text{NH}_3\text{PbX}_3$ , a Pb(II)-System with Cubic Perovskite Structure. *Z. Naturforsch.* **1978**, *33b*, 1443-1445.
- Kojima, A.; Teshima, K.; Shirai, Y.; Miyasaka, T. Organometal Halide Perovskites as Visible-Light Sensitizers for Photovoltaic Cells. *J. Am. Chem. Soc.* **2009**, *131*, 6050-6051.
- Kim, H.-S.; Lee, C.-R.; Im, J.-H.; Lee, K.-B.; Moehl, T.; Marchioro, A.; Moon, S.-J.; Humphry-Baker, R.; Yum, J.-H.; Moser, J. E.; et al. Lead Iodide Perovskite Sensitized All-Solid-State Submicron Thin Film Mesoscopic Solar Cell with Efficiency Exceeding 9%. *Sci. Rep.* **2012**, *2*, 591.
- Lee, M. M.; Teuscher, J.; Miyasaka, T.; Murakami, T. N.; Snaith, H. J. Efficient Hybrid Solar Cells Based on Meso-Structured Organometal Halide Perovskites. *Science* **2012**, *338*, 643-647.
- Im, J.-H.; Lee, C.-R.; Lee, J.-W.; Park, S.-W.; Park, N.-G. 6.5% Efficient Perovskite Quantum-Dot-Sensitized Solar Cell. *Nanoscale* **2011**, *3*, 4088-4093.
- Jeon, N. J.; Noh, J. H.; Kim, Y. C.; Yang, W. S.; Ryu, S.; Seok, S. I. Solvent Engineering for High-Performance Inorganic-Organic Hybrid Perovskite Solar Cells. *Nat. Mater.* **2014**, *13*, 897-903.
- Burschka, J.; Pellet, N.; Moon, S.-J.; Humphry-Baker, R.; Gao, P.; Nazeeruddin, M. K.; Grätzel, M. Sequential Deposition as a Route to High-Performance Perovskite-Sensitized Solar Cells. *Nature* **2013**, *499*, 316-319.
- Liu, M.; Johnston, M. B.; Snaith, H. J. Efficient Planar Heterojunction Perovskite Solar Cells by Vapour Deposition. *Nature* **2013**, *501*, 395-399.
- NREL. The Chart of Solar Cell Efficiency, [http://www.nrel.gov/ncpv/images/efficiency\\_chart.jpg](http://www.nrel.gov/ncpv/images/efficiency_chart.jpg).
- Noh, J. H.; Im, S. H.; Heo, J. H.; Mandal, T. N.; Seok, S. I. Chemical Management for Colorful, Efficient, and Stable Inorganic-Organic Hybrid Nanostructured Solar Cells. *Nano Lett.* **2013**, *13*, 1764-1769.
- Zhu, K.; Zhao, Y.  $\text{CH}_3\text{NH}_3\text{Cl}$ -Assisted One-Step Solution Growth of  $\text{CH}_3\text{NH}_3\text{PbI}_3$ : Structure, Charge-Carrier Dynamics, and Photovoltaic Properties of Perovskite Solar Cells. *J. Phys. Chem. C* **2014**, *118*, 9412-9418.
- Colella, S.; Mosconi, E.; Fedeli, P.; Listorti, A.; Gazza, F.; Orlandi, F.; Ferro, P.; Besagni, T.; Rizzo, A.; Calestani, G.; et al.  $\text{MAPbI}_{3-x}\text{Cl}_x$  Mixed Halide Perovskite for Hybrid Solar Cells: The Role of Chloride as Dopant on the Transport and Structural Properties. *Chem. Mater.* **2013**, *25*, 4613-4618.
- Eperon, G. E.; Stranks, S. D.; Menelaou, C.; Johnston, M. B.; Herz, L. M.; Snaith, H. J. Formamidinium Lead Trihalide: A Broadly Tunable Perovskite for Efficient Planar Heterojunction Solar Cells. *Energy Environ. Sci.* **2014**, *7*, 982-988.
- Mosconi, E.; Amat, A.; Nazeeruddin, M. K.; Grätzel, M.; Angelis, F. D. First-Principles Modeling of Mixed Halide Organometal Perovskites for Photovoltaic Applications. *J. Phys. Chem. C* **2013**, *117*, 13902-13913.
- Quarti, C.; Grancini, G.; Mosconi, E.; Bruno, P.; Ball, J. M.; Lee, M. M.; Snaith, H. J.; Petrozza, A.; Angelis, F. D. The Raman Spectrum of the  $\text{CH}_3\text{NH}_3\text{PbI}_3$  Hybrid Perovskite: Interplay of Theory and Experiment. *J. Phys. Chem. Lett.* **2014**, *5*, 279-284.
- Park, B.-w.; Philippe, B.; Gustafsson, T.; Sveinbjörnsson, K.; Hagfeldt, A.; Johansson, E. M. J.; Boschloo, G. Enhanced Crystallinity in Organic-Inorganic Lead Halide Perovskites on Mesoporous  $\text{TiO}_2$  via Disorder-Order Phase Transition. *Chem. Mater.* **2014**, *26*, 4466-4471.
- Chen, Q. i.; Zhou, H.; Song, T.-B.; Luo, S.; Hong, Z.; Duan, H.-S.; Dou, L.; Liu, Y.; Yang, Y. Controllable Self-Induced Passivation of Hybrid Lead Iodide Perovskites toward High Performance Solar Cells. *Nano Lett.* **2014**, *14*, 4158-4163.
- Frost, J. M.; Butler, K. T.; Brivio, F.; Hendon, C. H.; Schilfgaarde, M.; Walsh, A. Atomistic Origins of High-Performance in Hybrid Halide Perovskite Solar Cells. *Nano Lett.* **2014**, *14*, 2584-2590.
- Eremets, M. I.; Takemura, K.; Yusa, H.; Golberg, D.; Bando, Y.; Blank, V. D.; Sato, Y.; Watanabe, K. Disordered State in First-Order Phase Transitions: Hexagonal-to-Cubic and Cubic-to-Hexagonal Transitions in Boron Nitride. *Phys. Rev. B* **1998**, *57*, 5655.
- Binder, K. Theory of First-Order Phase Transitions. *Rep. Prog. Phys.* **1987**, *50*, 783-859.
- Even, J.; Pedesseau, L.; Jancu, J.-M.; Katan, C. Importance of Spin-Orbit Coupling in Hybrid Organic/Inorganic Perovskites for Photovoltaic Applications. *J. Phys. Chem. Lett.* **2013**, *4*, 2999-3005.
- De Boer, W. D. A. M.; Timmerma, D.; Dohnalová, K.; Yassievich, I. N.; Zhang, H.; Buma, W. J.; Gregorkiewicz, T. Red Spectral Shift and Enhanced Quantum Efficiency in Phonon-Free Photoluminescence from Silicon Nanocrystals. *Nat. Nanotechnol.* **2010**, *5*, 878-884.
- Riboli, F.; Caselli, N.; Vignolini, S.; Intonti, F.; Vynck, K.; Barthelemy, P.; Gerardino, A.; Balet, L.; Li, L. H.; Fiore, A.; Gurioli, M.; Wiersma, D. S. Engineering of Light Confinement in Strongly Scattering Disordered Media. *Nat. Mater.* **2014**, *13*, 720-725.
- Sadhanala, A.; Deschler, F.; Thomas, T. H.; Dutton, S. E.; Goedel, K. C.; Hanusch, F. C.; Lai, M. L.; Steiner, U.; Bein, T.; Docampo, P.; et al. Preparation of Single-Phase Films of  $\text{CH}_3\text{NH}_3\text{Pb}(\text{I}_{1-x}\text{Br}_x)_3$  with Sharp Optical Band Edges. *J. Phys. Chem. Lett.* **2014**, *5*, 2501-2505.
- Im, J.-H.; Chung, J.; Kim, S.-J.; Park, N.-G. Synthesis, Structure, and Photovoltaic Property of a Nanocrystalline 2H Perovskite-Type Novel Sensitizer  $(\text{CH}_3\text{CH}_2\text{NH}_3)\text{PbI}_3$ . *Nanoscale Res. Lett.* **2012**, *7*, 353.
- Schreiber, J.; Hildebrandt, S.; Kircher, W.; Richter, T. Optical Investigations of Surface and Interface Properties at III-V Semiconductors. *Mater. Sci. Eng.* **1991**, *B9*, 31-35.
- Anicete-Santos, M.; Orhan, E.; de Maura, M. A. M. A.; Simões, L. G. P.; Souza, A. G.; Pizani, P. S.; Leite, E. R.; Varela, J. A.; Andrés, J.; Beltrán, A.; et al. Contribution of Structural Order-Disorder to the Green Photoluminescence of  $\text{PbWO}_4$ . *Phys. Rev. B* **2007**, *75*, 165105.
- Blasse, G.; Corson, A. F. Electronic and Vibrational Spectra of Ordered Perovskites. *J. Solid State Chem.* **1973**, *6*, 513-518.
- Grancini, G.; Marras, S.; Prato, M.; Giannini, C.; Quarti, C.; Angelis, F. De; Bastiani, M. D.; Eperon, G. E.; Snaith, H. J.; Manna, L.; et al. The Impact of the Crystallization Processes on the Structural and Optical Properties of Hybrid Perovskite Films for Photovoltaics. *J. Phys. Chem. Lett.* **2014**, *5*, 279-284.
- Capozzi, V.; Fontana, A.; Fontana, M. P.; Mariotto, G.; Montagna, M.; Viliani, G. Raman Scattering in  $\text{PbI}_2$ . *Il Nuovo Cimento B* **1977**, *39*, 556-560.
- Coslovich, G.; Huber, B.; Lee, W.-S.; Chuang, Y.-D.; Zhu, Y.; Sasagawa, T.; Hussain, Z.; Bechtel, H. A.; Martin, M. C.; Shen, Z.-X.; et al. Ultrafast Charge Localization in a Stripe-Phase Nickelate. *Nat. Commun.* **2013**, *4*, 2643.

33. Frost, J. M.; Butler, K. T.; Brivio, F.; Hendon, C. H.; Van Schilfgaarde, M.; Walsh, A. Atomistic Origins of High-Performance in Hybrid Halide Perovskite Solar Cells. *Nano Lett.* **2014**, *14*, 2584–2590.
34. Umebayashi, T.; Asai, K.; Kondo, T.; Kakao, A. Electronic Structures of Lead Iodide Based Low-Dimensional Crystals. *Phys. Rev. B* **2003**, *67*, 155405.
35. Vermeulen, L. A.; Thompson, M. E. Stable Photo-Induced Charge Separation in Layered Viologen Compounds. *Nature* **1992**, *358*, 656–658.
36. Park, B.-w.; Yang, L.; Johansson, E. M. J.; Vlachopoulos, N.; Chams, A.; Perruchot, C.; Jouini, M.; Boschloo, G.; Hagfeldt, A. Neutral, Polaron, and Bipolaron States in PEDOT Prepared by Photoelectrochemical Polymerization and the Effect on Charge Generation Mechanism in the Solid-State Dye-Sensitized Solar Cell. *J. Phys. Chem. C* **2013**, *117*, 22484–22491.
37. Frisch, M. J.; Trucks, G. W.; Schlegel, H. B.; Scuseria, G. E.; Robb, M. A.; Cheeseman, J. R.; Scalmani, G.; Barone, V.; Mennucci, B.; Petersson, G. A. *et al. Gaussian 09*, Revision A.02; Gaussian, Inc.: Wallingford, CT, 2009.
38. Sanchez, R. S.; Gonzalez-Pedro, V.; Lee, J.-W.; Park, N.-G.; Kang, Y. S.; Mora-Sero, I.; Bisquert, J. Slow Dynamic Processes in Lead Halide Perovskite Solar Cells. Characteristic Times and Hysteresis. *J. Phys. Chem. Lett.* **2014**, *5*, 2357–2363.